



RESEARCH ARTICLE

WILEY

Estimation of event-based rainfall erosivity from radar after wildfire

Qinggaozi Zhu^{1,2,3} | Xihua Yang^{1,3} | Bofu Yu⁴ | Mitch Tulau³ | Sally McInnes-Clarke³ | Rachael H. Nolan^{2,7} | Zheyuan Du⁵ | Qiang Yu^{1,2,6}

¹State Key laboratory of Soil Erosion and Dryland Farming on the Loess Plateau, Northwest A&F University, Yangling 712100, Shaanxi, PR China

²School of Life Sciences, University of Technology Sydney, Sydney, NSW, Australia

³New South Wales Office of Environment and Heritage, Sydney South, NSW 1232, Australia

⁴Australian River Institute, School of Engineering, Griffith University, Nathan, QLD 4111, Australia

⁵School of Civil and Environmental Engineering, University of New South Wales, Randwick, NSW 2031, Australia

⁶College of Resources and Environment, University of Chinese Academy of Science, Beijing 100049, PR China

⁷Hawkesbury Institute for the Environment, Western Sydney University, Locked Bag 1797, Penrith, NSW 2751, Australia

Correspondence

Qinggaozi Zhu, State Key Laboratory of Soil Erosion and Dryland Farming on the Loess Plateau, Northwest A&F University, Yangling 712100, Shaanxi, PR China.

Email: Qinggaozi.Zhu@student.uts.edu.au

Funding information

National Natural Science Foundation of China, Grant/Award Number: 41730645; New South Wales Office of Environment and Heritage; State Key Laboratory of Soil Erosion and Dryland Farming on the Loess Plateau

Abstract

Rainfall erosivity impacts all stages of hillslope erosion processes and is an important factor (the 'R factor') in the Revised Universal Soil Loss Equation. It is estimated as the average annual value of the sum of all erosive events (EI_{30}) over a period of many years. For each storm event, the EI_{30} value is the product of storm energy, E in MJ ha^{-1} , and peak 30-min rainfall intensity (I_{30} , mm hr^{-1}). Previous studies often focused on estimation of the R factor for prediction of mean annual or long-term soil losses. However, many applications require EI_{30} values at much higher temporal resolution, such as postfire soil erosion monitoring, which requires a time step at storm events or on a daily basis. In this study, we explored the use of radar rainfall data to estimate the storm event-based EI_{30} after a severe wildfire in Warrumbungle National Park in eastern Australia. The radar-derived rainfall data were calibrated against 12 tipping bucket rain gauges across an area of 239 km^2 and subsequently used to produce a time series of rainfall erosivity maps at daily intervals since the wildfire in January 2013. The radar-derived daily rainfall showed good agreement with the gauge measurements ($R^2 > 0.70$, $E_c = 0.66$). This study reveals great variation in EI_{30} values ranging from near zero to $826.76 \text{ MJ}\cdot\text{mm}\cdot\text{ha}^{-1}\cdot\text{hr}^{-1}$ for a single storm event. We conclude that weather radar rainfall data can be used to derive timely EI_{30} and erosion information for fire incident management and erosion control. The methodology developed in this study is generic and thus readily applicable to other areas where weather radar data are available.

KEYWORDS

EI_{30} , postfire erosion, rainfall erosivity, storm events, weather radar

1 | INTRODUCTION

Hillslope erosion after a wildfire often causes land degradation and adversely impacts the environment and water quality (de Santos Loureiro & de Azevedo Coutinho, 2001; Klik, Haas, Dvorackova, & Fuller, 2015; Mello, Viola, Beskow, & Norton, 2013; Renard & Freimund, 1994). Individual high-intensity rainstorms can account for appreciable quantities of postfire erosion (Shakesby & Doerr, 2006). For example, in an early study in eucalypt forest near Sydney, Australia, Atkinson (1984) found that one rainfall event of 16.5 mm

lasting 45 min caused the equivalent of a year's loss of soil. Leitch, Flinn, and Van de Graaff (1983) estimated a loss of 22 t ha^{-1} after 21 mm of rain on small plots in burnt eucalypt-dominated forest in the Victorian Central Highlands of Australia.

It is therefore critical to monitor, map, and disseminate both average and more extreme erosion risks for catchments, given the predicted increase in climate variability and fire intensity in many parts of the world (Flannigan, Stocks, & Wotton, 2000; Moody, Shakesby, Robichaud, Cannon, & Martin, 2013; Westerling, Turner, Smithwick, Romme, & Ryan, 2011). Like cropping, (Van Oost, Govers, & Desmet,

2000), wildfire removes the soil cover and results in insufficient cover to protect soils, which are then vulnerable to an extreme erosive event. Hence, understanding the characteristics of the spatiotemporal distribution of wildfires and erosive rainfall events is critical.

Rainfall and runoff erosivity (the 'R factor') as defined in the Revised Universal Soil Loss Equation (Renard, Foster, Weesies, McCool, & Yoder, 1997) is the average annual value of the sum of all erosive events (El_{30}) over a period of many years. The R factor has been shown to be highly correlated with soil loss at many sites throughout the world (Panagos et al., 2017). For each storm event, the El_{30} value is the product of storm energy, E in MJ ha^{-1} , and peak 30-min rainfall intensity (I_{30} , mm hr^{-1} ; Renard et al., 1997; Wischmeier & Smith, 1958). Average monthly or annual rainfall erosivity has been assessed in several studies from long-term precipitation records and local rain gauges (de Santos Loureiro & de Azevedo Coutinho, 2001; Klik et al., 2015; Mello et al., 2013; Renard & Freimund, 1994). Some studies have discussed long-term rainfall erosivity impacts on hillslope erosion modeling at large spatial scales in Europe (Petan, Rusjan, Vidmar, & Mikoš, 2010), New Zealand (Klik et al., 2015), Japan (Santosa, Mitani, & Ikemi, 2010), and Africa (Vrieling, Sterk, & de Jong, 2010). Sidman, Guertin, Goodrich, Unkrich, and Burns (2016) have discussed the effect of postfire rainfall events on high-risk areas of flooding and erosion. Fischer et al. (2016) have estimated rainfall event erosivity by using radar data. However, there are few studies on the spatial and temporal variation of daily El_{30} during a postfire recovery period, despite the key role of erosivity in hillslope erosion.

Weather radar is one of the best sources to derive near real-time precipitation with high spatial and temporal resolution (few minutes to subhourly) for large areas (Seed, Siriwardena, Sun, Jordan, & Elliott, 2002; Wüest et al., 2010). It has been used to record real-time rainfall since the 1980s (Battan, 1973) and to provide estimation of spatio-temporal variability of erosivity (Fischer et al., 2016). Although radar offers high-resolution spatiotemporal rainfall data, its accuracy can be affected by certain weather types and technical limitations (Steiner, Smith, Burges, Alonso, & Darden, 1999). For example, limited visibility during particular weather events such as graupel and hail can affect the radar-received signal (Battan, 1973). Nevertheless, the adjusted radar-derived rainfall estimation can be very close to those obtained from rain gauges (Hossain, Anagnostou, Dinku, & Borga, 2004).

Weather radar measures the reflectivity (Z) and determines the rain rate (R) through a power law relationship of the formula $Z = aR^b$, known as the Z-R relationship (Seed et al., 2002; Steiner et al., 1999). The Z-R relationship normally varies by season and changes with the raindrop size distribution, the storm type (Chumchean, Seed, & Sharma, 2008), and the native climate (Seed et al., 2002); hence, radar rainfall estimation can be significantly affected by these factors, as well as the uncertainty or errors in reflectivity measurements. Alternative calibration methods include rain gauges and disdrometers (Angulo-Martínez, Beguería, & Kysely, 2016).

Gauge measurements are representative only at the measurement site (Steiner et al., 1999), whereas radar estimates instantaneous rainfall at some height above the ground (Steiner et al., 1999). Gauged rainfall measurements over a wider area have been applied to calibrate the Z-R relationship (Hasan, Sharma, Johnson, Mariethoz, & Seed, 2014). For example, Chumchean, Seed, and Sharma (2006) used a

Kalman filtering approach to calibrate the radar rainfall bias in real time in Australia; Rendon, Vieux, and Pathak (2012) adapted the adjustment to radar with seasonal variation in the United States; Bringi, Rico-Ramirez, and Thurai (2011) compared radar estimates against a gauge network in the United Kingdom; and Rozalis, Morin, Yair, and Price (2010) corrected radar by gauge rainfall to hydrological modeling in Europe.

Severe wildfire and subsequent storm events increase erosion rates, change runoff generation, and potentially contaminate water supplies due to the increased flux of sediment, nutrients, and other water constituents (Haberlandt, 2007). Severe wildfires removed the protective soil cover by vegetation and litter, changed soil aggregate stability and water repellency because of heating (Mataix-Solera, Cerdà, Arcenegui, Jordán, & Zavala, 2011), and have the potential to increase rainfall erosivity due to the loss of canopy (Nanko, Onda, Ito, & Moriwaki, 2008). Consequently, hillslope erosion rates may vary according to the burn severity, vegetation recovery, and the postfire rainfall events, though the relationship is not straightforward (Keeley, 2009; Moody et al., 2013; Vieira, Fernández, Vega, & Keizer, 2015). Therefore, quantitative and timely assessment of rainfall erosivity and hillslope erosion after wildfires during individual storm events is essential but remains a research challenge (Yin, Xie, Liu, & Nearing, 2015). This is largely due to the lack of quality rainfall data at high spatial and temporal resolutions at large spatial scales; the processing of these large spatial datasets itself is another challenge.

Key literature for the relevant studies are summarized in Table 1. This study focuses on the estimation of storm event-based El_{30} with the first attempt of using weather radar data to predict the near real-time rainfall erosivity in a burnt area after storm events. The specific objectives of this research were to (a) identify the bias-correction coefficient between radar rainfall and tipping-bucket gauge rainfall data; (b) estimate daily El_{30} and its spatial and temporal variation; and (c) assess the impact of event and daily El_{30} and apply them to near real-time monitoring of hillslope erosion risk. These objectives primarily define the structural subheadings in Sections 3, 4, and 5.

2 | STUDY SITE AND DATASETS

The study area for this research is approximately 450 km northwest of Sydney, centered on an area approximately 25 km west of Coonabarabran, and comprises Warrumbungle National Park (WNP) and the fire footprint (74,000 ha). The park ranges in elevation from 381 to 1,205 m. The climate is characterized by hot, usually humid summers and mild to cool winters. The nearest climate data come from Coonabarabran Airport Automatic Weather Station (AWS; BoM station no. 064017, -31.29° S, 149.07° E, elevation 645 m) and, until 2013, from Westmount (BoM station no. 064046, -33.33° S, 149.27° E, elevation 860 m) on the eastern boundary of the park, where the mean annual rainfall was 1,034 mm. The rainfall is summer-dominated, with January the wettest month, at 131 mm (Bureau of Meteorology, 2018b). The driest month is generally April, with a mean rainfall of 58 mm (Bureau of Meteorology, 2018b). Mean annual rainfall is much lower in the surrounding slopes and plains, at 670 mm (Bureau of Meteorology, 2018b).

TABLE 1 Summary of relevant studies using radar rainfall to estimate event erosivity in the burnt area

Study	Data/model used	Location/study size	Key results
1. Leitch et al. (1983)	Sampling and measurement.	Burnt forest near Warburton, Australia/ 0.35 km ²	(1) N/A (2) N/A (3) It was estimated that about 22 t ha ⁻¹ soil were washed after wildfire and the following intense thunderstorm (21 mm of rain).
2. Steiner et al. (1999)	WSR-88D radar (1 × 1 km ² , 5-min), rain gauge data/ Z–R relationship	Goodwin Creek, Mississippi, United States/21.4 km ²	(1) Radar rainfall estimates with a RMSE approximately 10% for the cumulative storm event of 30 mm or more. (2) N/A (3) N/A
3. Legates (2000)	WSR-88D weather radar (4 × 4 km ² , 5-min). 674 gauge-radar pairs over two months/ fixed Z–R relationship	The southern Great Plains, United States/ approximately 1,000 × 1,000 km ²	(1) $Z = 73.97 R^{1.409}$. Radar estimates provide the spatial variation to each storm while gauge measurements are applied to improve the accuracy. (2) N/A (3) N/A
4. Chumchean et al. (2006)	7-month radar and rain gauge data/Kalman filter	Sydney, Australia	(1) Kalman filter approach becomes unstable when the size of the gauging network decreases (less than one gauge 70 km ²) (2) N/A (3) N/A
5. Cruse et al. (2006)	NEXRAD radar (4 × 4 km ² , 15-min), 25 rain gauges, other data from NRI/WEPP model	Iowa, United States	(1) The correlation coefficient of monthly radar against 12 rain gauges from Iowa City network is around 0.9, RMSE about 0.12. While when compare to 12 rain gauges from Iowa State University Agriculture Network, correlation coefficient is around 0.7 and RMSE about 0.25. (2) Estimate spatial variation (10 × 10 km ²) of average runoff for a given day. (3) Soil erosion (unburnt) ranges from 0 to over 11.2 t ha ⁻¹ , which also spatially correlated with rainfall amounts.
6. Rozalis et al. (2010)	Radar rainfall (3 × 1 km ² , 5-min), 15 rain gauges, runoff from hydrometric station/hydrology model (SCS-CN)	Mediterranean watershed (unburnt) in Israel/27 km ²	(1) Radar-derived rainfall was calibrated from rain gauges. (2) N/A (3) According to the prediction from model, the flow magnitude was significantly affected by rain intensity distribution within the storm.
7. Vrieling et al. (2010)	TMPA daily and monthly rainfall, radar estimates (3 hr, 0.25°), rain gauges/modified Fournier Index (MFI)	Africa continent	(1) 3-hr radar-derived rainfall was not sufficient to represent high-intensity erosive events. (2) Monthly product provided spatial estimates of average annual erosivity. (3) N/A
8. Wüest et al. (2010)	72 rain gauges (10-min), Swiss weather radars (2 × 2 km ² , 5-min)	Swiss Plateau, Switzerland	(1) The error to intensity per hour and frequency were both less than 25%. (2) N/A (3) N/A
9. Nyman, Sheridan, Smith, and Lane (2011)	Radar-derived intensity (0.5 × 0.5 km ² , 10-min), manual rain gauges and debris flow sites from field survey/RUSLE model	Catchments in eastern Victoria, Australia/ <5 km ²	(1) Cumulative radar rainfall for debris flow was adjusted from the rainfall measured at field sites. (2) N/A (3) Debris flows triggered by intense storm events in burnt catchments when I_{30} ranged from 35 to 59 mm h ⁻¹ . Postfire sheet erosion from measurements indicates that hillslope material provides an important source of sediment.
10. Löwe, Thorndahl, Mikkelsen, Rasmussen, and Madsen (2014)	Radar (2 × 2 km ² , 10-min), six gauges (10-min) from the Danish SVK network and 2.5 months runoff data in summer/Z–R relationship, stochastic grey-box model	Two catchments in the Copenhagen, Denmark/13 and 30 km ² .	(1) $Z = 50 R^{1.8}$ (2) Correlation between rainfall and runoff forecasting has been estimated from both radar and gauge measurements. (3) N/A
11. Klik et al. (2015)	High-resolution rainfall data from 35 gauging station (10-min) /RUSLE model	New Zealand/ ~269,600 km ²	(1) N/A (2) The high variability of rainfall erosivity is mainly associated with the climatic and topographic differences across New Zealand. The average storm-based erosivity in summer is 2.1-times more than that from winter. The peak erosivities appear mostly in summer (December to February) (3) N/A

NSW, Australia

(Continues)

TABLE 1 (Continued)

Study	Data/model used	Location/study size	Key results
12. Yang and Yu (2014)	Gridded daily rainfall from BoM, 124 sites pluviography rainfall data/RUSLE model		(1) N/A (2) In terms of the same rain in the same month, the rainfall erosivity is higher at lower latitude and at lower elevation (3) N/A
13. Fischer et al. (2016)	Radar rainfall ($1 \times 1 \text{ km}^2$, 5-min) from RADOLAN and 30 rain gauges/USLE and RUSLE2 model	Bavarian Tertiary Hills, Germany/ $\sim 15,000 \text{ km}^2$	(1) Adjust radar rainfall in 60-min interval from 30 rain gauges (mean difference 4%, RMSE is 3 mm) (2) The difference of event rainfall erosivity between adjacent cells is up to 120 N h^{-1} . Compare with the daily rainfall, the spatiotemporal variation is considerably stronger. (3) N/A
14. Sidman et al. (2016)	USGS stream gauges, DHR radar/KINEROS2, AGWA model	North Creek within Zion National Park, United States/ 243.83 km^2	(1) Rainfall representation by using radar was applied in areas with low-gauge density. (2) N/A (3) The varying rainfall representation has a great impact on the peak flow when modeling runoff after wildfire, although not significantly affected the predictions for hotspot areas.
15. This study	Radar rainfall from BoM ($1 \times 1 \text{ km}^2$, 10-min, 256×256), twelve rain gauges from field, / RUSLE model	Warrumbungle National Park, Australia/ 233 km^2	(1) The radar-derived rainfall indicates strong positive correlation with the gauge measurements ($R^2 = 0.75$). (2) There is great seasonal variation in spatial and temporal distributions of E_{30} across the Park. Maximum event E_{30} was estimated about $827 \text{ MJ mm-ha}^{-1} \text{ hr}^{-1}$. (3) The maximum erosion rate from soil plot measurement is approximately $1.35 \text{ t-ha}^{-1}\cdot\text{yr}^{-1}$ on average across the WNP. The time series of daily E_{30} maps can provide timely information for erosion control and monitoring of fire recovery.

Note. Not all papers included soil erosion modeling and postfire assessment via radar images, and these are denoted with an N/A representing 'not applicable' in the relevant part of the "Key results" column. In the "Key results" column, the abovementioned three components are identified by the code: (1) identify bias correction and radar rainfall variation in the relationship between gauge and radar rainfall; (2) estimate E_{30} and its temporal and spatial variation; and (3) assess impact of E_{30} on soil erosion in the burnt area.

A severe wildfire ignited in WNP, New South Wales (NSW), Australia, on January 12, 2013. Under the extreme fire weather, 95% of the park was burnt, with 72% of the area categorized as high to extreme burn severity. Fire severity was estimated from RapidEye images based on normalized burn ratio methods (Battan, 1973) and categorized into four classes (0: unburnt; 1: low severity; 2: high severity; 3: extreme severity; Storey, 2014). Later, on February 1, 2013, an intense storm event (rainfall intensity $>50 \text{ mm h}^{-1}$) occurred, followed by several other storms where 100–150 mm of rain fell over the burnt area. These events led to extraordinary erosion and long-term landscape changes to this iconic park.

A series of 12 closed plots were established in early 2014 at locations across WNP in order to monitor soil erosion and groundcover. These plots were established in May 2014 with a size approximately 9 m^2 as recommended by Riley, Crozier, and Blong (1981). Though smaller than the standard USLE plot (length = 22.1 m, slope = 9%), they were easier to install and maintain and allowed for comparison with previous studies in Australia (e.g., Atkinson, 1984; Atkinson, 2012; Yang et al., 2018). These monitoring sites were visited at approximately 2-month intervals from May 2014 (19 times in total). Accumulated sediment was collected during each field visit and sent to Yanco Natural Resources Laboratory, where the material was dried and weighed, and particle size classes and soil texture determined (Table 2). From July 2015, each plot site or nearby had a standard rain gauge and a tipping bucket rain gauge installed from which rainfall

intensity could be measured. Figure 1 shows the locations of the 12 soil plots and the tipping bucket rain gauges, and the basic information of these plots are listed in Table 2.

In Australia, weather radar networks have been operated by the Australia Bureau of Meteorology (BoM) since 1948. Nevertheless, the first quantitative rainfall estimation by radar was not published and analyzed until the 1960s (Seed et al., 2002). There are 43 full-time weather radar stations across Australia; each one updates images at 10-min intervals with a domain of $256 \times 256 \text{ km}^2$ and a spatial resolution of 1 km. For this study, the Namoi (Blackjack Mountain) S-band radar (DWSR 8502S; -31.0240° S , 150.1915° E) data (10-min, 1 km) were obtained from the BoM. Continuous radar images were obtained for the period from January to March 2013 immediately after fire and an extended period from January 2014 to June 2017 for ongoing monitoring.

3 | METHODS

3.1 | Radar data processing and bias correction

To calculate the radar-derived rainfall accumulation, the raw radar reflectivity measurements (10-min, $1 \times 1 \text{ km}$) obtained from the Namoi station are firstly corrected by removing the effect of beam blocking. Then rainfall accumulation is converted from the corrected

TABLE 2 Basic information of the twelve soil plots within the Warrumbungle National Park

Site	Easting	Northing	Name	Elevation (m)	Fire	Geology	Aspect (degree)	Slope (%)	Clay (%)	Silt (%)	Fine sand (%)	Coarse Sand (%)
1	148.9546	-31.3575	Gunneemooroo	595	0	V	240	30	27	13	30	30
2	149.0322	-31.3249	Strathmore lower	608	1	V	330	25	21	27	29	23
3	148.9947	-31.2617	Buckleys West	445	3	S	65	32	11	7	26	56
4	148.9929	-31.2491	Nth fire trail lower	715	2	V	260	22	15	35	24	26
5	148.9885	-31.2380	Nth fire trail upper	692	2	V	180	22	18	26	36	20
6	148.9916	-31.2477	Nth fire trail middle	605	2	V	220	25	13	44	22	21
7	149.0099	-31.2865	Middle Valley	447	1	S	135	25	13	9	28	50
8	149.0119	-31.2879	Scabilon Hill	519	3	S	250	37	13	33	22	32
9	149.0247	-31.3423	TV Tower	1040	1	V	70	38	8	34	26	32
10	149.0343	-31.3260	Strathmore upper	687	1	V	30	25	22	17	22	39
11	149.0778	-31.2693	Siding Spring	1023	2	V	340	18	19	35	19	27
12	149.0089	-31.2767	Blackman	509	2	S	190	22	14	10	30	46

Note. Fire: fire severity (0–3 represent unburnt to severe burnt classes), S: sandstone, V: volcanic.

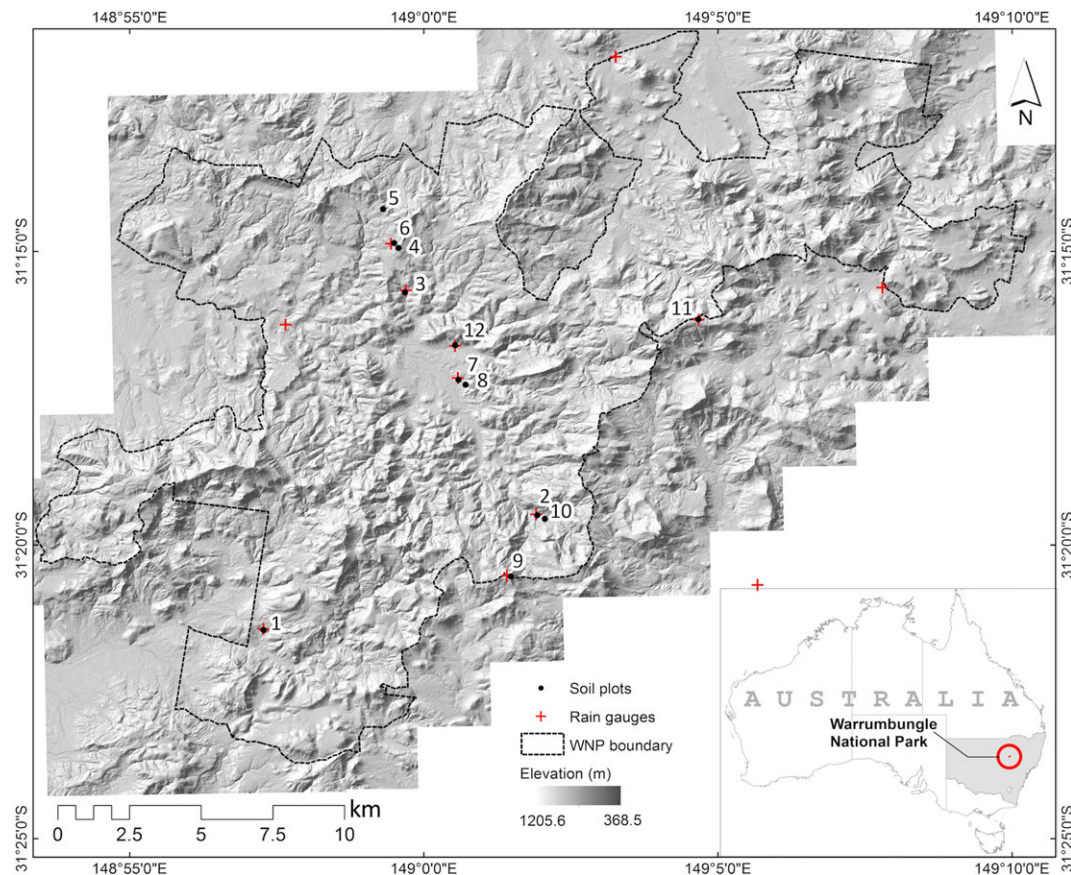


FIGURE 1 The Warrumbungle National Park study area and the locations of soil plots and tipping-bucket rain gauges [Colour figure can be viewed at wileyonlinelibrary.com]

radar reflectivity through a Z–R relationship as shown below (Bureau of Meteorology, 2018a),

$$Z = 60 R^{1.7}, \quad (1)$$

where Z represents the reflectivity and R is the rain rate per pixel. BoM keeps this Z–R relationship constant rather than varying it by season, as there are insufficient gauges to conduct a real-time

adjustment within the Namoi coverage area. In this study, daily radar-derived rainfall estimations were adjusted against daily rain gauge observations through linear regression once the radar reflectivity was converted to rainfall accumulation and daily rainfall depth rate.

The procedures for the rain gauge adjustment are illustrated in Figure 2. Radar-based rainfall accumulations were first gap-filled by linear interpolation with data from neighboring time steps. MATLAB scripts were then developed and applied to batch convert the original

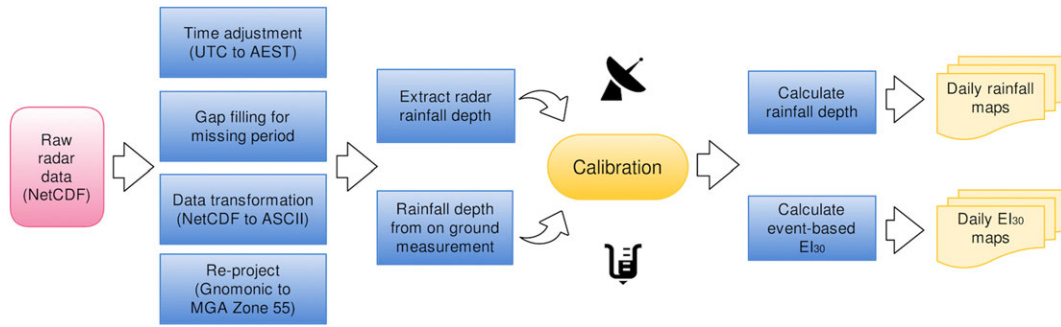


FIGURE 2 Processing steps of radar rainfall [Colour figure can be viewed at wileyonlinelibrary.com]

radar data in NetCDF format to ESRI ASCII grids, which were then input to ArcGIS for extraction of rainfall accumulation and further calculations for EI_{30} . To ensure data consistency, the radar data were reprojected from Gnomonic to MGA Zone 55 so that all datasets were in the same coordinate system. Also, Coordinated Universal Time in the radar data was readjusted to local Australian Eastern Standard Time (Australian Eastern Standard Time = Coordinated Universal Time + 10:00).

The 12 tipping buckets gauges installed within WNP were used to calibrate the weather radar rainfall data. Where there were data gaps due to rain gauge instrument failure (<15.5%), the missing values were filled from the most appropriate gauge according to linear regression and comparison with all the surrounding rain gauges.

Bias removal is one of the most important processes in the radar-based rainfall estimation. To adjust the radar rainfall bias, we developed a linear relationship between rainfall measured from rain gauges and the radar. This relationship was based on daily rainfall amounts (July 2015 to June 2017) for reasons that (a) there was too much variation and data gaps in the 10-min rainfall time series and (b) the final EI_{30} maps are on a daily basis.

3.2 | Event-based EI_{30} estimation

The EI_{30} for a single storm event is the value of energy, E in MJ ha^{-1} , multiplied by the peak 30-min rainfall intensity I_{30} (mm hr^{-1}). In this study, E is computed from the 10-min radar-based rainfall in 10-min intervals following Equation 2.

$$E = \sum_{r=1}^N e_r \Delta V_r, \quad (2)$$

$$e_r = 0.29 \left[1 - 0.72 \exp\left(-a \frac{\Delta V_r}{\Delta t_r}\right) \right], \quad (3)$$

where $\Delta V_r / \Delta t_r$ is the rainfall intensity (mm hr^{-1}), whereas ΔV_r refers to rainfall amount during that particular period, Δt_r , N is the number of 10-min intervals (e.g., $N = 3$ for 30-min), e_r ($\text{MJ ha}^{-1} \text{mm}^{-1}$) means unit kinetic energy, and a is an empirical coefficient. This form of the equation, including empirical coefficients, was based on the work of Kinnell (1981). Equation 3 was proposed by Brown and Foster (1987) as a replacement for the original equation presented in the *Agriculture Handbook* No.537 (Wischmeier & Smith, 1978) and further modified by Foster et al. (2003) as part of RUSLE2. The maximum unit energy was taken as 0.29 based on the work of Rosewell (1986). The difference of these two equations is that the revised exponent value

(0.082) is slightly higher than the counterpart value (0.05) of Brown and Foster (1987). It is believed that this kinetic energy and intensity (KE-I) coefficient (Brown & Foster, 1987) underestimates the rainfall erosivity by about 10% (Nearing, Yin, Borrelli, & Polyakov, 2017; Renard & Freimund, 1994). Thus, in this study, we compared daily EI_{30} computed from Brown and Foster (1987; RUSLE) with its revised version (Foster et al., 2003; RUSLE2).

The rainfall intensity for 30-min (mm hr^{-1}) intervals I_{30} is calculated as follows:

$$I_{30} = P_{30} \times 2, \quad (4)$$

where P_{30} is the maximum 30-min rainfall depth (mm). It is multiplied by 2 to convert to an hourly scale. Peak rainfall amounts in 30-min intervals was extracted from radar images at every three 10-min intervals. Renard et al. (1997) recommended including all storm events in the R factor calculation. Most literature has defined erosive storm events as cumulative rainfall events greater than 12.7 mm, that is, at least 12.7 mm rain within 30-min, and separated by a break of more than 6 hr. However, the discrepancy in the calculated R factor due to different rainfall thresholds increases as the mean annual rainfall decreases because the relative contribution of small storm events to the R factor increases in dry areas (Yu, 1999). Hence, the threshold was set as 5 mm d^{-1} instead of 12.7 mm in this study to ensure that small events that did not produce runoff were not included in the determination of daily erosivity.

3.3 | Model performance and erosion risk assessment

Once event-based EI_{30} values were computed from the radar data at 10-min intervals, these values were accumulated to total daily, monthly, and annual rainfall erosivity (R factor). Model performance was measured by the coefficient of efficiency, E_c (Nash & Sutcliffe, 1970), which is commonly used to assess model performance in hydrology and soil sciences (Loague & Freeze, 1985; Risse, Nearing, Lafen, & Nicks, 1993):

$$E_c = 1 - \frac{\sum_{i=1}^M (y_i - \hat{y})^2}{\sum_{i=1}^M (y_i - \bar{y})^2}, \quad (5)$$

where y_i are observed values while \hat{y} are modelled values, \bar{y} is the average of observed values, and M represented the sample size. Essentially, E_c is an indicator of how close the scatter of predicted versus actual values are to the 1:1 line (Yang, Yu, & Xie, 2015). The common coefficient of determination (R^2), root mean square difference (RMSE), and

standard error of the mean were also applied to assess model performances by comparing the plot values (e.g., gauged rainfall data) with the simulated values estimated by weather radar and the KE-I relationship.

4 | RESULTS

4.1 | Bias correction and radar rainfall variation

Time series of daily rainfall (>5 mm d⁻¹) from July 2015 to June 2017 (two hydrological years) were compared with different data sources

(Figure 3) including (a) pluviograph data from AWS (064017) at every 6-min and (b) mean rainfall amount from the 12 tipping-bucket rain gauges. The comparisons show that there is a good relationship between radar-derived rainfall and the gauge rainfall measurements. The relationship between raw radar and gauged rainfall during two hydrological years when combined is relatively weak (Figure 3c, $R^2 = 0.5$, $E_c = 0.043$) compared with the individual relationships for each hydrological year separately (Figure 3a,b, $R^2 > 0.7$). The weaker relationship with the pluviograph data ($R^2 = 0.45$) might be due to the location of the pluviograph station (AWS 064017), which is about 30 km away from most of the rain gauges. For this reason, we only

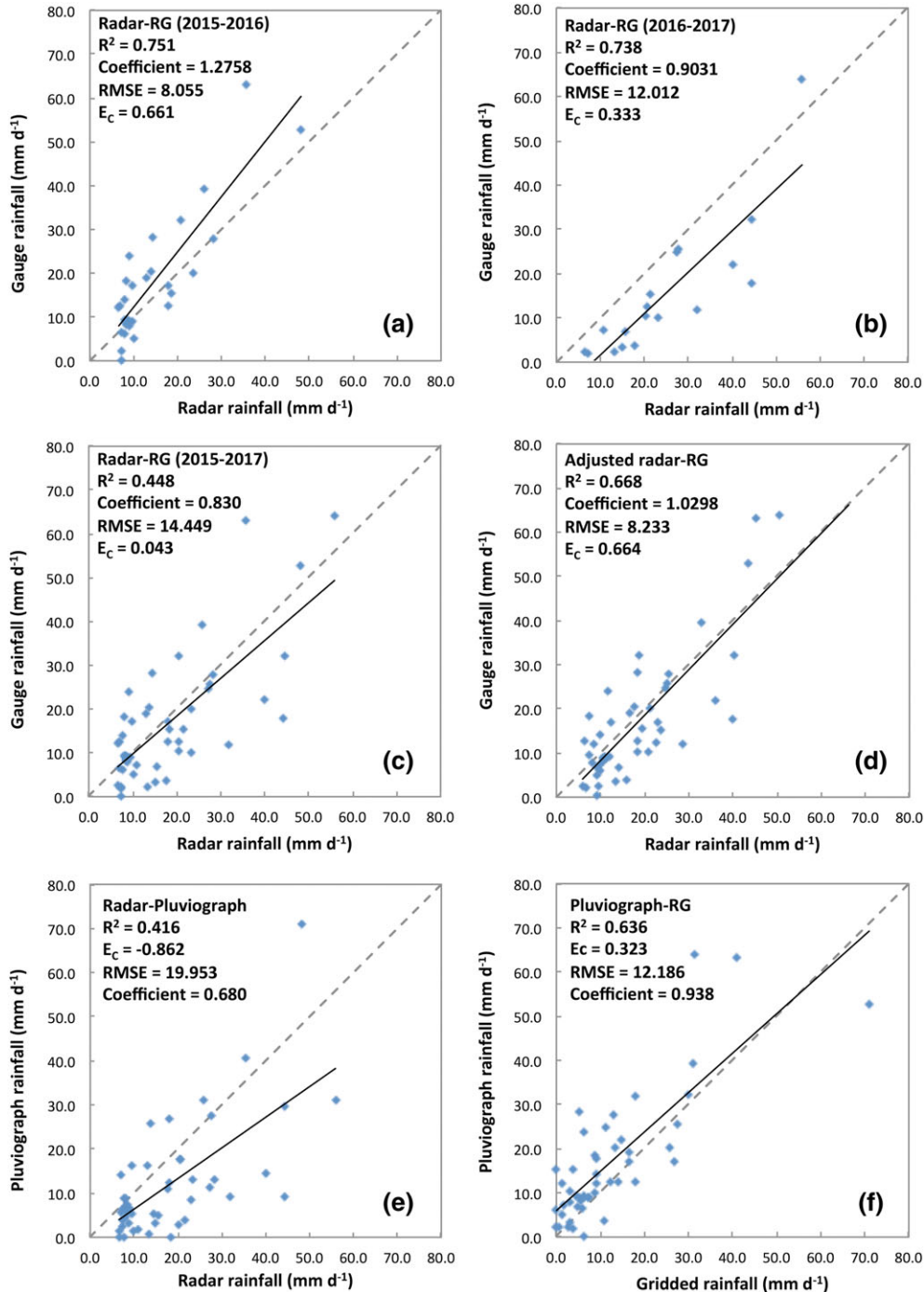


FIGURE 3 Relationship between radar-derived, gauge-measured, and pluviograph rainfall [Colour figure can be viewed at wileyonlinelibrary.com]

used the rain gauge data for the bias correction, and the pluviograph data were only used as complementary data sources when gauge data were not available, such as immediately after the wildfire in 2013 (Figure 3e,f), because gauges were not installed in WNP until July 2015.

An adjustment factor (AF) was applied to calibrate the radar-based estimates pixel by pixel and for all radar data with 10-min time step:

$$R_{gauge} = AF \times R_{radar}, \quad (6)$$

where R_{gauge} is the daily rainfall collected from the tipping bucket rain gauges on the ground, AF is the adjustment factor, and R_{radar} is the radar-based rainfall extracted from the pixel in which the gauge is located. Two AFs were applied (corresponding to the two hydrological years). For the 2015–2016 hydrological year, an AF of 1.28 was applied (Figure 3a), whereas for the 2016–2017 hydrological year, an AF of 0.90 was applied (Figure 3b). For the regressions used to derive both AFs, there was a strong correlation between gauge and radar-derived rainfall ($R^2 = 0.74$ – 0.75 , $RMSE = 8.06$ – 1201 , $E_c = 0.33$ – 0.66).

After calibration against the gauges in WNP (Figure 3d), time series rainfall depth maps derived from the radar data were produced at hourly, daily, and monthly intervals. Figure 4 shows examples of daily rainfall derived from the radar data when the daily rainfall amount was more than 5 mm. The daily rainfall amounts were accumulations over the previous 24 hr to 9:00 a.m. local time. The peak radar rainfall was estimated to be as high as 61.87 mm for February 2, 2013. Hotspot areas with large daily rainfall amounts coincided with areas of extreme burn severity (e.g., on February 18, 19, 2, and 22 and March 5, 2013). These calibrated rainfall data were subsequently used for EI_{30} calculations and compared with observed soil loss from hillslope plots on a monthly time step.

4.2 | EI_{30} and its temporal and spatial variation

The modelled daily EI_{30} over two hydrological years follows a similar trend to rainfall in general, irrespective of which data sources (radar or gauge rainfall) or methods (KE–I relation from RUSLE or RUSLE2) were used (Figure 5a–d). The results show a strong agreement ($R^2 = 0.80$, $n = 52$) between the radar-based EI_{30} and the gauge-based

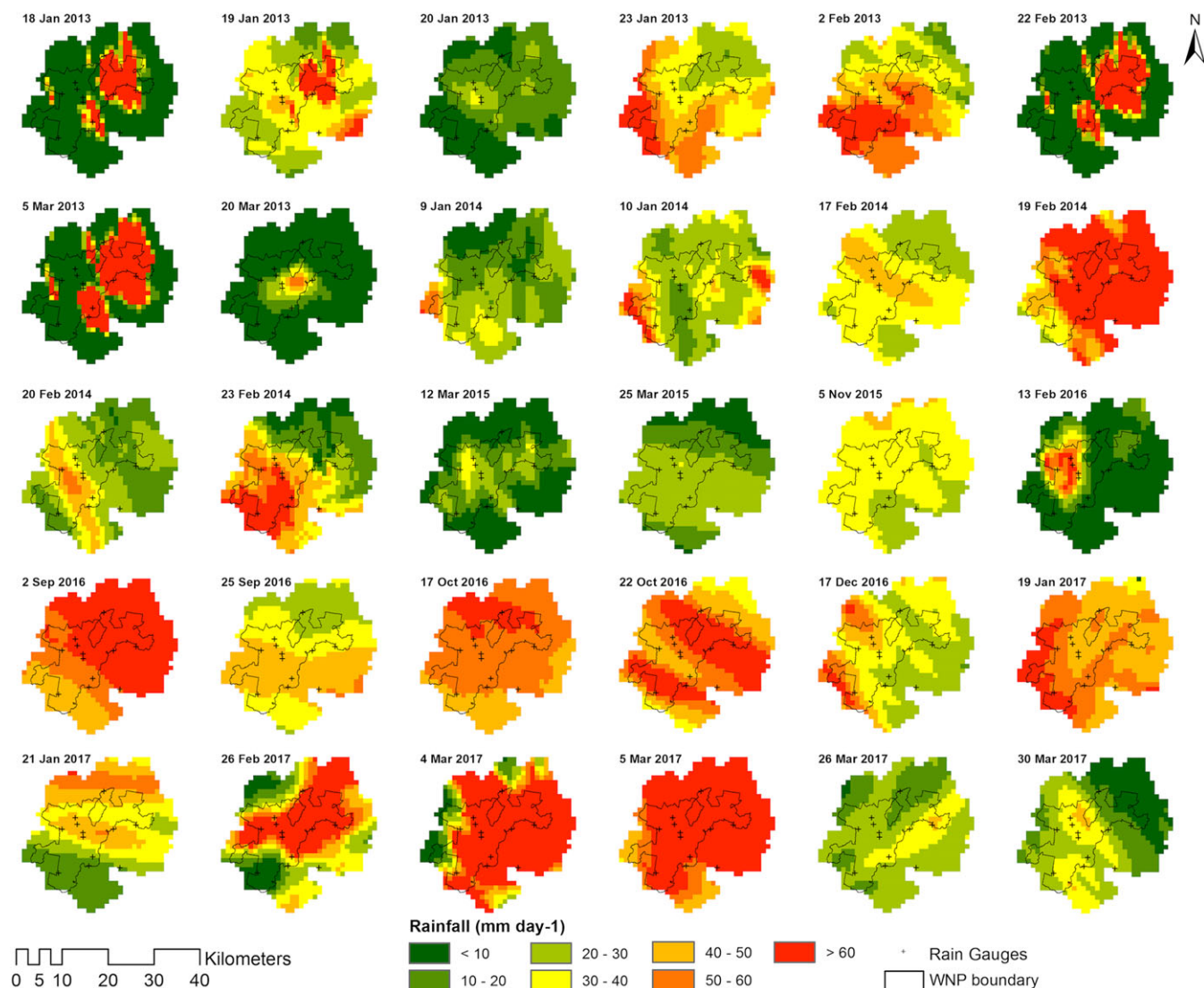


FIGURE 4 Radar-derived daily rainfall after calibration from January 2013 to June 2017. The shape here is actually the fire ground for selected storm events [Colour figure can be viewed at wileyonlinelibrary.com]

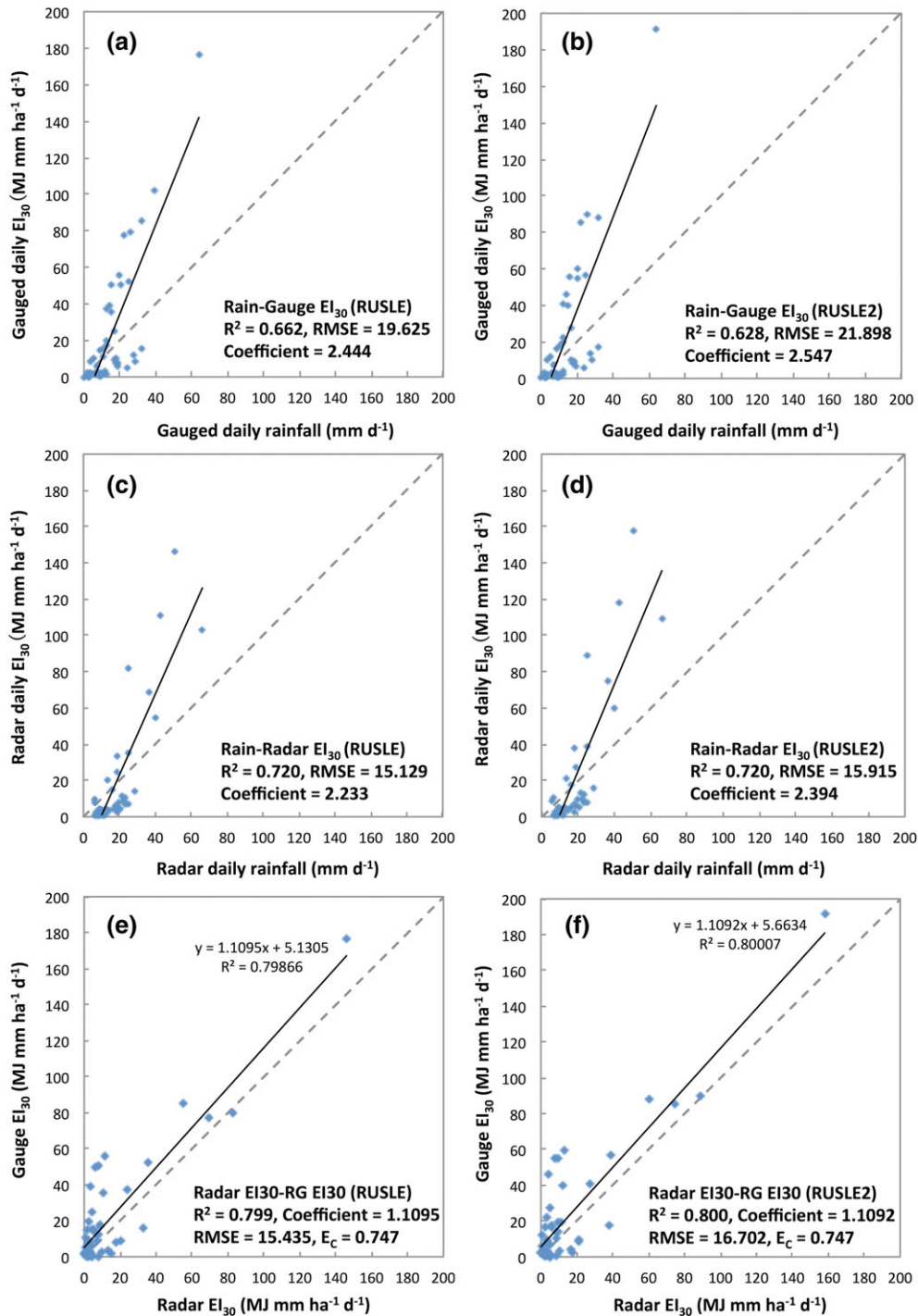


FIGURE 5 (a) Regression of gauge daily rainfall and gauge daily EI_{30} (coefficient: 0.05); (b) regression of gauge daily rainfall and gauge daily EI_{30} (coefficient: 0.082); (c) regression of radar daily rainfall and radar-derived daily EI_{30} (coefficient: 0.05); (d) regression of radar daily rainfall and radar-derived daily EI_{30} (coefficient: 0.082); (e) comparison of daily EI_{30} (coefficient: 0.05) from radar rainfall gauge measurement; (f) comparison of daily EI_{30} (coefficient: 0.082) from radar rainfall gauge measurement [Colour figure can be viewed at wileyonlinelibrary.com]

EI_{30} , although the radar-derived data (coefficient: 0.05) underestimated the daily EI_{30} by approximately 8.20% compared with the daily EI_{30} , when estimated using the 0.082 KE-I coefficient.

To examine seasonal variation, monthly EI_{30} values were accumulated from daily radar-derived EI_{30} values and compared against the monthly EI_{30} values calculated from the gauge sites and pluviograph data. Table 3 shows the similar seasonal variation in EI_{30} from all these different data sources. The higher EI_{30} values appeared in summer (December, January, and February), with the EI_{30} values in winter

(June, July, and August) significantly lower. These trends are reflected in all EI_{30} estimates from radar, gauges, and pluviograph measurements.

For the storm event on February 1, 2013, between 12:30 p.m. and 13:30 p.m., there were noticeable differences in absolute values between pluviograph and radar-derived event EI_{30} . As shown in Table 3, the event radar EI_{30} during the storm accounts for more than 9% of seasonal EI_{30} for the three summer months (December to February). In contrast, for the pluviograph data, the EI_{30} estimated from

TABLE 3 Seasonal variation of $E_{I_{30}}$ and storm event assessment on February 1, 2013

Seasonal $E_{I_{30}}$ (RUSLE)	July 2015–June 2016			July 2016–June 2017			20130201 12:30–13:30			Rain			$E_{I_{30}}$ (RUSLE)			$E_{I_{30}}$ (RUSLEZ)			
	RG	Radar	Pluviograph	RG	Radar	Pluviograph	RG	Radar	Pluviograph	Pluviograph	Radar	Pluviograph	Radar	Pluviograph	Radar	Pluviograph	Radar	Pluviograph	Radar
Summer	42.49%	31.55%	38.12%	24.44%	29.43%	35.90%				91.62%	86.95%	99.89%	88.65%	99.87%	86.89%				
Autumn	19.93%	23.18%	18.95%	33.46%	28.51%	38.46%				50.50%	29.13%	80.67%	31.22%	79.45%	31.11%				
Winter	12.00%	21.52%	7.15%	10.31%	11.55%	2.01%				10.94%	8.03%	53.75%	9.28%	56.26%	10.18%				
Spring	25.58%	23.75%	35.78%	31.78%	30.50%	23.63%				5.91%	-	37.63%	-	35.23%	-				
Summer & Autumn	62.42%	54.73%	57.07%	57.90%	57.94%	74.36%				21.67%	27.56%	66.63%	29.72%	70.81%	32.73%				
Spring & Summer	68.07%	55.29%	73.90%	56.23%	59.94%	59.53%				53.96%	-	70.01%	-	62.62%	-				

the same event accounts for more than 50% of the seasonal El_{30} for summer months. Event-based El_{30} was largely consistent with the radar-derived rainfall; each peak El_{30} value corresponds to the peak rainfall intensity (Figure 4). For any given time step (e.g., daily and monthly), the predicted rainfall erosivity varied spatially across the park. The El_{30} fluctuated in response to the radar-derived rainfall estimates.

Figure 6 shows the daily El_{30} of storm events and their spatial variation over the monitoring period (January 2013 to June 2017). These maps can be used to identify potential high erosion risk areas during storm events. For example, the daily El_{30} variation on March 4, 2017 in Figure 6 refers to a daily El_{30} value as high as $826.76 \text{ MJ mm ha}^{-1} \text{ hr}^{-1}$ for a single event.

4.3 | Impact of El_{30} on erosion

The measured erosion during each field visit follows a similar seasonal pattern to the monthly El_{30} in general (Figure 7), irrespective of which data source was applied (radar or gauge). Among the soil plots across

the park, high erosivity was apparent at Site 1 and Site 11 as shown on Figure 7. Areas near these sites had experienced stronger storm events and flash flooding than most other soil plots. The higher cumulative El_{30} values resulted in higher soil losses from the soil plots.

The relationship between the annual sum of El_{30} and postfire erosion was compared and assessed at soil plot sites from July 2015 (Figure 7). The measured soil loss at each plot reflects the influence of El_{30} , but there is an obvious discrepancy between observed soil loss and El_{30} values. For example, the highest erosion rates were measured at Site 11; however, the corresponding El_{30} was not the highest. Heavy rainfall occurred near Site 2, but the measured erosion rates from that soil plot were relatively low.

There exists a statistical difference of erosion rates according to the burn severity from the twelve measured erosion plots installed in 2014 (Table 4). Higher erosion occurred in extremely burnt area within one year after the wildfire (Table 4), but such consistency became weaker in subsequent years (2016–2017, Table 4) due to vegetation recovery and erosion control measures. Site 1 (unburnt) has higher erosion rate compared with some burned areas (e.g., low severity

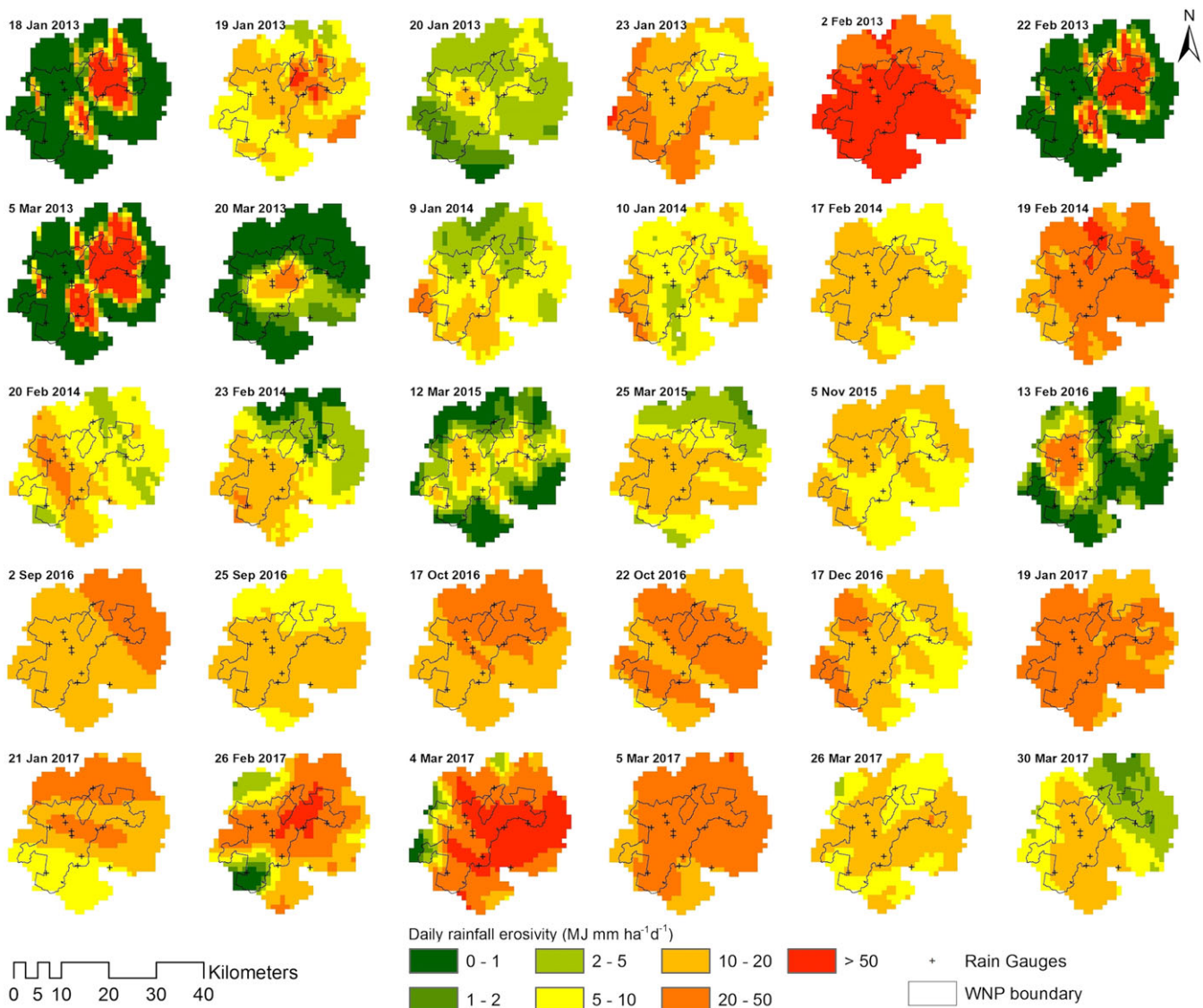


FIGURE 6 Time series El_{30} maps and the spatial variations in the monitoring period from January 2013 to June 2017. El_{30} distribution here was actually the annual estimation from the single storm event [Colour figure can be viewed at wileyonlinelibrary.com]

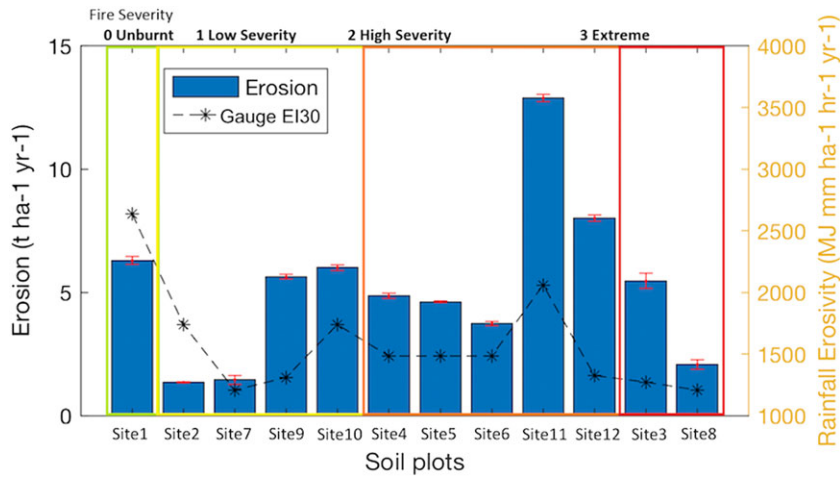


FIGURE 7 Spatial variation of rainfall erosivity and erosion [Colour figure can be viewed at wileyonlinelibrary.com]

TABLE 4 The influence of EI_{30} ($\text{MJ mm ha}^{-1} \text{hr}^{-1} \text{yr}^{-1}$) on site erosion ($\text{t ha}^{-1} \text{yr}^{-1}$) at different fire severity classes

Fire severity	Sites	Average EI_{30} ($\text{MJ mm ha}^{-1} \text{hr}^{-1} \text{yr}^{-1}$)	Average field erosion ($n = 19$) ($\text{t ha}^{-1} \text{yr}^{-1}$)	Annual field erosion ($\text{t ha}^{-1} \text{yr}^{-1}$)					
				2014–2015 ($n = 8$)		2015–2016 ($n = 8$)		2016–2017 ($n = 3$)	
				Mean	SEM	Mean	SEM	Mean	SEM
Unburnt	1	2777.00	1.00	1.59	-	0.46	-	0.87	-
Low severity	2, 7, 9, and 10	1620.85	0.60	1.07	0.25	0.27	0.08	0.48	0.21
High severity	4, 5, 6, 11, and 12	1657.55	1.03	1.60	0.58	0.63	0.14	0.59	0.22
Extreme severity	3 and 8	1354.13	1.12	2.19	0.32	0.42	0.19	0.13	0.06

class) due to its higher rainfall erosivity which is approximately two times higher than the low severity sites (2, 7, 9, and 10). In the burn severity classification, there is essentially no difference between the 'unburnt' and 'low severity' classes as long as the groundcover is concerned. Therefore, other factors (EI_{30} , slopes) might be more influential in erosion than groundcover for these classes. This finding also suggests the needs for an unambiguous classification as proposed by Vieira et al. (2015), and they highlighted the incoherencies between existing burn severity classifications and concluded that different burn severity does not evidence significant differences in postfire runoff.

5 | DISCUSSION

5.1 | Bias correction and radar rainfall variation

Radar rainfall can play a significant role in representing rainfall intensity, especially in areas without a high density of gauge networks (Hossain et al., 2004; Sidman et al., 2016). Even where rain gauges or pluviograph rainfall stations exist, they are unlikely to replace radar-derived rainfall estimates, due to high spatial and temporal resolution from radar data.

The tipping bucket gauges measured the rainfall depth across the WNP and provided precise calibration and supplementary observation for radar estimation (Legates, 2000). However, the rainfall gauges are sparse and thus unable to identify all the hotspot areas across the park without the assistance of the radar-derived rainfall. This also limited the application of the Kalman filter in calibration of radar rainfall as it requires a much higher density of gauges (about one gauge per 70 km^2 ; Chumchean et al., 2006).

The pluviographic rainfall data from the Coonabarabran Airport AWS (064017) was available at 6-min intervals from January 2013 to present. In contrast, the 12 rain gauges were installed in the WNP only since July 2015; thus, the pluviographic rainfall data are as essential as the radar-derived rainfall for estimating the daily rainfall erosivity immediately after wildfire (since January 2013).

The results from this study illustrate that there is a strong positive correlation between radar-derived rainfall and daily EI_{30} ($R^2 = 0.72$). Higher radar rainfall estimates correspond to greater rainfall erosivity at the same grid cell. The variation of rainfall mirrors the variation of EI_{30} particularly in the severely burnt area. In agreement with Sidman et al. (2016), the varying rainfall has a great impact on peak rainfall erosivity modeling.

5.2 | EI_{30} and its temporal and spatial variation

Seasonal variation of rainfall erosivity is apparent due to the large seasonal variation of rainfall amount and intensity. The highest seasonal EI_{30} occurred in summer, with the lowest in winter. This seasonal trend agrees with our previous studies using long historical rainfall records which show strong seasonality with the highest rainfall erosivity in summer and lowest in winter (Renard et al., 1997).

Compared with daily rainfall, the spatiotemporal variation of rainfall erosivity was considerably larger (Fischer et al., 2016). From our results, the average seasonal EI_{30} in summer is approximately two to three times greater than that predicted in winter, based on radar estimation and gauge measurements respectively. In comparison, Yang et al. (2015) reported that the R factor between summer and winter had about seven-fold difference in NSW statewide. Klik et al. (2015)

found that rainfall erosivity in summer was 2.1 times higher than that from winter in New Zealand, modelled from gauged rainfall.

Spatial distribution is a highly important factor when estimating erosivity and erosion in burnt area as wildfire removes the soil cover and creates a potential window for extreme erosion events (e.g., storm events). Radar EI_{30} revealed that the spatial variation of daily EI_{30} is mostly driven by the spatial variations in rainfall (Figure 5c,d) and explicitly predicted the high-risk areas due to a particular event (Figure 6).

In this study, radar data have been first applied to detect high-risk areas and temporal variation of daily EI_{30} (Figure 6). However, daily EI_{30} estimated using RUSLE was underestimated by 8.20% in comparison to that from RUSLE2 (Figure 5e). This underestimation agrees with Nearing et al. (2017) and Foster et al. (2003), who believed that the KE-I relationship from RUSLE underestimates the rainfall erosivity by approximately 10%. Despite changing the coefficient to 0.082 instead of the commonly applied 0.05 in RUSLE2 (Foster et al., 2003), the radar-derived daily EI_{30} was still underestimated by 11% (Figure 5f) compared with the gauge-estimated EI_{30} . Nevertheless, it is worth noting that no matter which coefficient has been used, they were both developed based on experiments and data collected in the United States. Furthermore, although an absolute difference exists among different KE-I relations, these slight differences will not significantly affect the estimated results for the WNP study. Thus, we continue to use the KE-I relationship proposed by Brown and Foster (1987) in the following sections. Another possible explanation for the discrepancy might be due to the gap period of the radar estimation, which may miss some rainfall events, whereas the point-based gauge measurement fills the gap of radar rainfall.

5.3 | Impact of EI_{30} on postfire erosion

Similar seasonal variation was apparent from the time series of erosion measurements and monthly EI_{30} (Figure 7). More soil loss was observed in summer when heavy rainstorms occurred, whereas less erosion was measured in the dry winters. In general, higher erosion rates were positively correlated with fire severity; however, relatively high erosion rates were also evident in some unburnt areas such as Site 1. This discrepancy is probably due to the vegetation recovery of burnt areas and the effects of other RUSLE factors such as soil, rainfall, and topographic factors. For example, the slope steepness factor for Site 1 was measured as high as 0.3 (Table 2) with the highest rainfall erosivity among the 12 sites (Table 4).

The average erosion from plots in extremely burnt areas decreased by about 94.1% from 2014 ($2.19 \text{ t ha}^{-1} \text{ yr}^{-1}$) to 2017 ($0.13 \text{ t ha}^{-1} \text{ yr}^{-1}$). In comparison, the erosion changes in low (1.07 to $0.48 \text{ t ha}^{-1} \text{ yr}^{-1}$) and high severity (1.60 to $0.59 \text{ t ha}^{-1} \text{ yr}^{-1}$) burn areas over three years gradually decreased by 55.0% and 63.1%, respectively. One explanation for these differences is that the rapid vegetation recovery in high severity burn areas (Gordon, Price, Tasker, & Denham, 2017) leads to a reduction of postfire erosion rates (Table 4). The groundcover in WNP has been generally increasing since the fire in early February 2013 and returned to near preburn levels within 1 year (Yang et al., 2018). There is an increasing trend from May 2014 (73%) to July 2017 (79%) according to the

groundcover measurements, although the groundcover varies seasonally. Gordon et al. (2017) observed strong positive associations between *Acacia* species in WNP and total midstory vegetation cover and fire severity. Results from this study also showed that the groundcover had recovered 1–1.5 years after the fire, and the level of groundcover has continued to gradually improved ever since (to July 2017). The enhanced postfire erosion is not directly and solely a result of fire severity, but it also related to a combination of the spatial distribution of rainfall and other erosion factors (e.g., groundcover and soil properties). This was further complicated by changes in these factors on different time scales (Moody et al., 2013). Thus, mapping the burn severity, and not just the fire footprint, combined with radar-based event EI_{30} provides high spatiotemporal resolution information in relation to fire regime management.

RUSLE or the revised model (RUSLE2) was originally designed to predict average annual soil loss. Both models have limitations for post-fire erosion modeling; in particular, they are unable to account for changes in soil hydrophobicity, which can affect sediment runoff and often temporarily increases after fire (Sheridan, Lane, & Noske, 2007). As such, these models have limitations in predicting hillslope erosion for a particular storm event. However, some alternative process-based models such as WEPP (Nearing, Foster, Lane, & Finkner, 1989) are extremely sensitive to parameter estimations, and those predictions are often poor (Van Oost et al., 2000), whereas RUSLE requires low data inputs, is robust, and has widely been used across the world. It is possible to estimate daily (or storm event-based) soil loss with time series EI_{30} at a subdaily scale as discussed above or the product of the runoff ratio (Q_R) and EI_{30} index (Kinnell, 2010; Kinnell, 2014) given the fact that soil erodibility and topographic factors are stable and groundcover factor changes seasonally (Yang et al., 2018).

Prediction of event-based EI_{30} will be increasingly important due to the higher likelihood of intense storm events under climate change (Alexander et al., 2007). The current climate change projections predict that the region is trending towards an increased risk of wildfire due to warmer and drier conditions (Hennessy et al., 2005; Pitman, Narisma, & McAneney, 2007) and higher frequencies of extreme weather such as storm events (Alexander et al., 2007; Nyman et al., 2011).

6 | CONCLUSIONS

In this study, we have assessed various rainfall data types covering various periods, including pluviograph rainfall, tipping bucket rain gauges, and radar-derived rainfall estimates for their potential for estimating EI_{30} . It is important to choose the most suitable rainfall data to fill the gaps and simulate the time series of rainfall erosivity into WNP after the wildfire. Radar-derived rainfall data has its advantage in spatial and temporal resolutions. Thus, the exploration of radar rainfall data in estimating EI_{30} is of great importance when rainfall erosivity and postfire erosion estimation at a storm event or daily time step is required.

We have developed a set methodology to estimate EI_{30} , compared with the actual erosion from soil plots at subdaily temporal

resolutions and provided timely information for park management on erosion control. Our study has demonstrated that weather radar underestimated rainfall by a factor of 1.28 ($R^2 = 0.75$) from July 2015 to June 2016 and overestimated rainfall ($AF = 0.90$, $R^2 = 0.74$) from July 2016 to June 2017 but shows strong correlation with gauged rainfall. El_{30} for storm events or on a daily basis can be estimated from the radar-based rainfall time series at high temporal resolution.

Our results indicate that the highest seasonal El_{30} appeared in summer whereas the lowest in winter. Hillslope erosion rates in general follow similar seasonality. The time series radar-derived El_{30} demonstrate the potential high-risk erosion areas on each rain day. The change of postfire erosion to some extent is mostly driven by the fire severity. The measured soil loss rates at soil plots correspond well with the El_{30} estimates in the same periods. Our results provide evidence to support and promote the use of weather radar technology for estimation of rainfall erosivity for individual storm events. As rainfall erosivity is one of the key factors in causing land degradation at a range of scales, this study reveals the potential in using weather radars for real-time or nearly real-time monitoring and prediction of land degradation around the world. Outcomes from this study have been directly used in hillslope erosion monitoring across the WNP at near real time (Yang et al., 2018). Our methodology and scripts are general, thus applicable for areas where weather radar data available.

ACKNOWLEDGEMENTS

This study was supported by National Natural Science Foundation of China (41730645) and Special-Funds of Scientific Research Programs of State Key Laboratory of Soil Erosion and Dryland Farming on the Loess Plateau (No. A314021403-1703). We thank the New South Wales Office of Environment and Heritage (OEH) for providing funding and data for the Warrumbungle National Park fire recovery research project and our subproject on Soil and Water. The Bureau of Meteorology provided radar rainfall data. We thank Dr. Alan Seed for his patient advice on weather radar data. Many staff in the NSW National Park and Wildlife Services, in particular, Craig Wall, provided assistance for fieldwork and advice. Colleagues in Soil and Water, Fire Behavior, Vegetation and Fauna teams provided useful discussion and advice to our subproject. OEH scientists Ms. Robin McAlpine and Dr. Senani Karunaratne assisted with fieldwork on groundcover and remote sensing measurements.

ORCID

Qinggaazi Zhu  <http://orcid.org/0000-0002-2371-4626>

Rachael H. Nolan  <http://orcid.org/0000-0001-9277-5142>

REFERENCES

- Alexander, L. V., Hope, P., Collins, D., Trewin, B., Lynch, A., & Nicholls, N. (2007). Trends in Australia's climate means and extremes: A global context. *Australian Meteorological Magazine*, 56(1), 1-18. <https://doi.org/10.1.1.222.5972&rep=rep1&type=pdf>
- Angulo-Martínez, M., Beguería, S., & Kysely, J. (2016). Use of disdrometer data to evaluate the relationship of rainfall kinetic energy and intensity (KE-I). *Science of the Total Environment*, 568, 83-94. <https://doi.org/10.1016/j.scitotenv.2016.05.223>
- Atkinson, G. (1984). Erosion damage following bushfires. *Journal of Soil Conservation New South Wales (Australia)*. <http://escholarship.library.usyd.edu.au/journals/index.php/LIN>
- Atkinson, G. (2012). Soil erosion following wildfire in Royal National Park, NSW. Paper presented at the Proceedings of the Linnean Society of New South Wales 134, B25-B38. <http://escholarship.library.usyd.edu.au/journals/index.php/LIN>
- Battan, L. J. (1973). Radar observation of the atmosphere. *Quarterly Journal of the Royal Meteorological Society*. <https://doi.org/10.1002/qj.49709942229>
- Bringi, V., Rico-Ramirez, M., & Thurai, M. (2011). Rainfall estimation with an operational polarimetric C-band radar in the United Kingdom: Comparison with a gauge network and error analysis. *Journal of Hydrometeorology*, 12(5), 935-954. <https://doi.org/10.1175/JHM-D-10-05013.1>
- Brown, L., & Foster, G. (1987). Storm erosivity using idealized intensity distributions. *Transactions of the ASAE*, 30(2), 379-0386. <https://doi.org/10.13031/2013.31957>
- Bureau of Meteorology (2018a). How radar-derived rainfall accumulations are calculated. Retrieved from http://www.bom.gov.au/australia/radar/about/calculating_rainfall_accumulations.shtml
- Bureau of Meteorology (2018b). Monthly rainfall for Coonabarabran (Westmount). Retrieved from http://www.bom.gov.au/jsp/ncc/cdio/weatherData/av?p_nccObsCode=139&p_display_type=dataFile&p_startYear=&p_c=&p_stn_num=064046
- Chumchuan, S., Seed, A., & Sharma, A. (2006). Correcting of real-time radar rainfall bias using a Kalman filtering approach. *Journal of Hydrology*, 317(1), 123-137. <https://doi.org/10.1016/j.jhydrol.2005.05.013>
- Chumchuan, S., Seed, A., & Sharma, A. (2008). An operational approach for classifying storms in real-time radar rainfall estimation. *Journal of Hydrology*, 363, 1, 1-1, 17. <https://doi.org/10.1016/j.jhydrol.2008.09.005>
- Cruse, R., Flanagan, D., Frankenberger, J., Gelder, B., Herzmann, D., James, D., ... Opsomer, J. (2006). Daily estimates of rainfall, water runoff, and soil erosion in Iowa. *Journal of Soil and Water Conservation*, 61(4), 191-199. <http://www.jswconline.org/content/61/4/191.short>
- de Santos Loureiro, N., & de Azevedo Coutinho, M. (2001). A new procedure to estimate the RUSLE EI 30 index, based on monthly rainfall data and applied to the Algarve region, Portugal. *Journal of Hydrology*, 250(1), 12-18. [https://doi.org/10.1016/S0022-1694\(01\)00387-0](https://doi.org/10.1016/S0022-1694(01)00387-0)
- Fischer, F., Hauck, J., Brandhuber, R., Weigl, E., Maier, H., & Auerswald, K. (2016). Spatio-temporal variability of erosivity estimated from highly resolved and adjusted radar rain data (RADOLAN). *Agricultural and Forest Meteorology*, 223, 72-80. <https://doi.org/10.1016/j.agrformet.2016.03.024>
- Flannigan, M. D., Stocks, B. J., & Wotton, B. M. (2000). Climate change and forest fires. *Science of the Total Environment*, 262(3), 221-229. [https://doi.org/10.1016/S0048-9697\(00\)00524-6](https://doi.org/10.1016/S0048-9697(00)00524-6)
- Foster, G., Yoder, D., Weesies, G., McCool, D., McGregor, K., & Bingner, R. (2003). RUSLE 2.0 user's guide. *USDA-Agricultural Research Service*, Washington, DC. <https://www.tucson.ars.ag.gov/unit/Publications/PDFfiles/1117.pdf>
- Gordon, C. E., Price, O. F., Tasker, E. M., & Denham, A. J. (2017). Acacia shrubs respond positively to high severity wildfire: Implications for conservation and fuel hazard management. *Science of the Total Environment*, 575, 858-868. <https://doi.org/10.1016/j.scitotenv.2016.09.129>
- Haberlandt, U. (2007). Geostatistical interpolation of hourly precipitation from rain gauges and radar for a large-scale extreme rainfall event. *Journal of Hydrology*, 332(1), 144-157. <https://doi.org/10.1016/j.jhydrol.2006.06.028>
- Hasan, M. M., Sharma, A., Johnson, F., Mariethoz, G., & Seed, A. (2014). Correcting bias in radar Z-R relationships due to uncertainty in point rain gauge networks. *Journal of Hydrology*, 519, 1668-1676. <https://doi.org/10.1016/j.jhydrol.2014.09.060>
- Hennessy, K., Lucas, C., Nicholls, N., Bathols, J., Suppiah, R., & Ricketts, J. (2005). Climate change impacts on fire-weather in south-east Australia.

- Climate Impacts Group, CSIRO Atmospheric Research and the Australian Government Bureau of Meteorology, Aspendale. http://www.cmar.csiro.au/e-print/open/hennessykyj_2005b.pdf
- Hossain, F., Anagnostou, E. N., Dinku, T., & Borga, M. (2004). Hydrological model sensitivity to parameter and radar rainfall estimation uncertainty. *Hydrological Processes*, 18(17), 3277–3291. <https://doi.org/10.1002/hyp.5659>
- Keeley, J. E. (2009). Fire intensity, fire severity and burn severity: A brief review and suggested usage. *International Journal of Wildland Fire*, 18, 116–126. <https://doi.org/10.1071/WF07049>
- Kinnell, P. (1981). Rainfall intensity-kinetic energy relationships for soil loss prediction. *Soil Science Society of America Journal*, 45(1), 153–155. <https://doi.org/10.2136/sssaj1981.03615995004500010033x>
- Kinnell, P. (2010). Event soil loss, runoff and the Universal Soil Loss Equation family of models: A review. *Journal of Hydrology*, 385(1), 384–397. <https://doi.org/10.1016/j.jhydrol.2010.01.024>
- Kinnell, P. (2014). Modelling event soil losses using the $Q_R E_{I30}$ index within RUSLE2. *Hydrological Processes*, 28(5), 2761–2771. <https://doi.org/10.1002/hyp.9790>
- Klik, A., Haas, K., Dvorackova, A., & Fuller, I. C. (2015). Spatial and temporal distribution of rainfall erosivity in New Zealand. *Soil Research*, 53(7), 815–825. <https://doi.org/10.1071/SR14363>
- Legates, D. R. (2000). Real-time calibration of radar precipitation estimates. *The Professional Geographer*, 52(2), 235–246. <https://doi.org/10.1111/0033-0124.00221>
- Leitch, C., Flinn, D. W., & Van de Graaff, R. (1983). Erosion and nutrient loss resulting from Ash Wednesday (February 1983) wildfires a case study. *Australian Forestry*, 46(3), 173–180. <https://doi.org/10.1080/00049158.1983.10674396>
- Loague, K. M., & Freeze, R. A. (1985). A comparison of rainfall-runoff modeling techniques on small upland catchments. *Water Resources Research*, 21(2), 229–248. <https://doi.org/10.1029/WR021i002p00229>
- Löwe, R., Thorndahl, S., Mikkelsen, P. S., Rasmussen, M. R., & Madsen, H. (2014). Probabilistic online runoff forecasting for urban catchments using inputs from rain gauges as well as statically and dynamically adjusted weather radar. *Journal of Hydrology*, 512, 397–407. <https://doi.org/10.1016/j.jhydrol.2014.03.027>
- Mataix-Solera, J., Cerdà, A., Arcenegui, V., Jordán, A., & Zavala, L. M. (2011). Fire effects on soil aggregation: A review. *Earth-Science Reviews*, 109(1–2), 44–60. <https://doi.org/10.1016/j.earscirev.2011.08.002>
- Mello, C. R., Viola, M. R., Beskow, S., & Norton, L. D. (2013). Multivariate models for annual rainfall erosivity in Brazil. *Geoderma*, 202, 88–102. <https://doi.org/10.1016/j.geoderma.2013.03.009>
- Moody, J. A., Shakesby, R. A., Robichaud, P. R., Cannon, S. H., & Martin, D. A. (2013). Current research issues related to post-wildfire runoff and erosion processes. *Earth-Science Reviews*, 122, 10–37. <https://doi.org/10.1016/j.earscirev.2013.03.004>
- Nanko, K., Onda, Y., Ito, A., & Moriwaki, H. (2008). Effect of canopy thickness and canopy saturation on the amount and kinetic energy of throughfall: An experimental approach. *Geophysical Research Letters*, 35(5). <https://doi.org/10.1029/2007GL033010>
- Nash, J. E., & Sutcliffe, J. V. (1970). River flow forecasting through conceptual models part I—A discussion of principles. *Journal of Hydrology*, 10(3), 282–290. [https://doi.org/10.1016/0022-1694\(70\)90255-6](https://doi.org/10.1016/0022-1694(70)90255-6)
- Nearing, M., Foster, G., Lane, L., & Finkner, S. (1989). A process-based soil erosion model for USDA-Water Erosion Prediction Project technology. *Transactions of the ASAE*, 32(5), 1587–1593. <https://doi.org/10.13031/2013.31195>
- Nearing, M., Yin, S.-q., Borrelli, P., & Polyakov, V. O. (2017). Rainfall erosivity: An historical review. *Catena*, 157, 357–362. <https://doi.org/10.1016/j.catena.2017.06.004>
- Nyman, P., Sheridan, G. J., Smith, H. G., & Lane, P. N. (2011). Evidence of debris flow occurrence after wildfire in upland catchments of south-east Australia. *Geomorphology*, 125(3), 383–401. <https://doi.org/10.1016/j.geomorph.2010.10.016>
- Panagos, P., Borrelli, P., Meusburger, K., Yu, B., Klik, A., Lim, K. J., ... Chattopadhyay, N. (2017). Global rainfall erosivity assessment based on high-temporal resolution rainfall records. *Scientific Reports*, 7(1), 4175. <https://doi.org/10.1038/s41598-017-04282-8>
- Petan, S., Rusjan, S., Vidmar, A., & Mikoš, M. (2010). The rainfall kinetic energy-intensity relationship for rainfall erosivity estimation in the mediterranean part of Slovenia. *Journal of Hydrology*, 391(3), 314–321. <https://doi.org/10.1016/j.jhydrol.2010.07.031>
- Pitman, A., Narisma, G., & McAneney, J. (2007). The impact of climate change on the risk of forest and grassland fires in Australia. *Climatic Change*, 84(3–4), 383–401. <https://doi.org/10.1007/s10584-007-9243-6>
- Renard, K. G., Foster, G. R., Weesies, G., McCool, D., & Yoder, D. (1997). Predicting soil erosion by water: A guide to conservation planning with the Revised Universal Soil Loss Equation (RUSLE) (Vol. 703): US Government Printing Office Washington, DC. <https://naldc.nal.usda.gov/download/11126/PDF>
- Renard, K. G., & Freimund, J. R. (1994). Using monthly precipitation data to estimate the R-factor in the revised USLE. *Journal of Hydrology*, 157(1), 287–306. [https://doi.org/10.1016/0022-1694\(94\)90110-4](https://doi.org/10.1016/0022-1694(94)90110-4)
- Rendon, S. H., Vieux, B. E., & Pathak, C. S. (2012). Continuous forecasting and evaluation of derived Z-R relationships in a sparse rain gauge network using NEXRAD. *Journal of Hydrologic Engineering*, 18(2), 175–182. [https://doi.org/10.1061/\(ASCE\)HE.1943-5584.0000579](https://doi.org/10.1061/(ASCE)HE.1943-5584.0000579)
- Riley, S., Crozier, P., & Blong, R. (1981). An inexpensive and easily installed runoff plot. *Journal of the Soil Conservation Service of New South Wales*, 37(3), 144–147. <http://agris.fao.org/agris-search/search.do?recordID=US201301992895>
- Risse, L., Nearing, M., Lafen, J., & Nicks, A. (1993). Error assessment in the universal soil loss equation. *Soil Science Society of America Journal*, 57(3), 825–833. <https://doi.org/10.2136/sssaj1993.03615995005700030032x>
- Rosewell, C. J. (1986). Rainfall kinetic energy in eastern Australia. *Journal of Climate and Applied Meteorology*, 25(11), 1695–1701. [http://doi.org/10.1175/1520-0450\(1986\)025<1695:RKEIEA>2.0.CO;2](http://doi.org/10.1175/1520-0450(1986)025<1695:RKEIEA>2.0.CO;2)
- Rozalis, S., Morin, E., Yair, Y., & Price, C. (2010). Flash flood prediction using an uncalibrated hydrological model and radar rainfall data in a Mediterranean watershed under changing hydrological conditions. *Journal of Hydrology*, 394(1), 245–255. <https://doi.org/10.1016/j.jhydrol.2010.03.021>
- Santosa, P. B., Mitani, Y., & Ikemi, H. (2010). Estimation of RUSLE EI 30 based on 10 min interval rainfall data and GIS-based development of rainfall erosivity maps for Hitotsuse basin in Kyushu Japan. Paper presented at the 2010 18th International Conference on Geoinformatics. <https://doi.org/10.1109/GEOINFORMATICS.2010.5568195>
- Seed, A., Siriwardena, L., Sun, X., Jordan, P., & Elliott, J. (2002). On the calibration of Australian weather radars. *CRC for Catchment Hydrology*. <https://ewater.org.au/archive/crcch/archive/pubs/pdfs/technical200207.pdf>
- Shakesby, R., & Doerr, S. (2006). Wildfire as a hydrological and geomorphological agent. *Earth-Science Reviews*, 74(3), 269–307. <https://doi.org/10.1016/j.earscirev.2005.10.006>
- Sheridan, G. J., Lane, P. N., & Noske, P. J. (2007). Quantification of hillslope runoff and erosion processes before and after wildfire in a wet Eucalyptus forest. *Journal of Hydrology*, 343(1–2), 12–28. <https://doi.org/10.1016/j.jhydrol.2007.06.005>
- Sidman, G., Guertin, D. P., Goodrich, D. C., Unkrich, C. L., & Burns, I. S. (2016). Risk assessment of post-wildfire hydrological response in semi-arid basins: The effects of varying rainfall representations in the KINEROS2/AGWA model. *International Journal of Wildland Fire*, 25(3), 268–278. <https://doi.org/10.1071/WF14071>
- Steiner, M., Smith, J. A., Burges, S. J., Alonso, C. V., & Darden, R. W. (1999). Effect of bias adjustment and rain gauge data quality control on radar

- rainfall estimation. *Water Resources Research*, 35(8), 2487–2503. <https://doi.org/10.1029/1999WR900142>
- Storey, M. (2014). *Fire severity mapping for the Wambelong 2013 fire*. CERMB: University of Wollongong.
- Van Oost, K., Govers, G., & Desmet, P. (2000). Evaluating the effects of changes in landscape structure on soil erosion by water and tillage. *Landscape Ecology*, 15(6), 577–589. <https://doi.org/10.1023/A:1008198215674>
- Vieira, D. C. S., Fernández, C., Vega, J. A., & Keizer, J. J. (2015). Does soil burn severity affect the post-fire runoff and interrill erosion response? A review based on meta-analysis of field rainfall simulation data. *Journal of Hydrology*, 523, 452–464. <https://doi.org/10.1016/j.jhydrol.2015.01.071>
- Vrieling, A., Sterk, G., & de Jong, S. M. (2010). Satellite-based estimation of rainfall erosivity for Africa. *Journal of Hydrology*, 395(3), 235–241. <https://doi.org/10.1016/j.jhydrol.2010.10.035>
- Westerling, A. L., Turner, M. G., Smithwick, E. A., Romme, W. H., & Ryan, M. G. (2011). Continued warming could transform Greater Yellowstone fire regimes by mid-21st century. *Proceedings of the National Academy of Sciences*, 108(32), 13165–13170. <https://doi.org/10.1073/pnas.1110199108>
- Wischmeier, W. H., & Smith, D. D. (1958). Rainfall energy and its relationship to soil loss. *Eos, Transactions American Geophysical Union*, 39(2), 285–291. <https://doi.org/10.1029/TR039i002p00285>
- Wischmeier, W. H., & Smith, D. D. (1978). Predicting rainfall erosion losses—A guide to conservation planning. <https://www.cabdirect.org/cabdirect/abstract/19786726437>
- Wüest, M., Frei, C., Altenhoff, A., Hagen, M., Litschi, M., & Schär, C. (2010). A gridded hourly precipitation dataset for Switzerland using rain-gauge analysis and radar-based disaggregation. *International Journal of Climatology*, 30(12), 1764–1775. <https://doi.org/10.1002/joc.2025>
- Yang, X., & Yu, B. (2014). Modelling and mapping rainfall erosivity in New South Wales. *Soil Research*. <https://doi.org/10.1071/SR14188>
- Yang, X., Yu, B., & Xie, X. (2015). Predicting changes of rainfall erosivity and hillslope erosion risk across greater Sydney region, Australia. *International Journal of Geospatial and Environmental Research*, 2(1), 2. <https://dc.uwm.edu/ijger/vol2/iss1/2>
- Yang, X., Zhu, Q., Tulan, M., McInnes-Clarke, S., Sun, L., & Zhang, X. P. (2018). Near real-time monitoring of post-fire hillslope erosion in a burnt national park after storm events. *International Journal of Wildland Fire*. <https://doi.org/10.1071/WF18011> (Online early)
- Yin, S.-q., Xie, Y., Liu, B., & Nearing, M. (2015). Rainfall erosivity estimation based on rainfall data collected over a range of temporal resolutions. *Hydrology and Earth System Sciences*, 19(10), 4113. <https://doi.org/10.5194/hess-19-4113-2015>
- Yu, B. (1999). A comparison of the R-factor in the Universal Soil Loss Equation and revised universal soil loss equation. *Transactions of the ASAE*, 42(6), 1615. <https://doi.org/10.13031/2013.13327>

How to cite this article: Zhu Q, Yang X, Yu B, et al. Estimation of event-based rainfall erosivity from radar after wildfire. *Land Degrad Dev*. 2019;30:33–48. <https://doi.org/10.1002/ldr.3146>